Supporting Information

Broedersz et al. 10.1073/pnas.1402529111

1. Monte Carlo Simulation of a Lattice Model for DNA with Interacting DNA-Binding Proteins

We used a Monte Carlo procedure to simulate the equilibrium conformations of DNA with interacting DNA-bound proteins. In our model, the DNA is described as a linear, self-avoiding chain on a cubic lattice in 3D. For simplicity, the DNA is taken to be coarse-grained at the scale of a protein-binding site, ℓ_0, so that exactly one protein can bind the DNA per site of the cubic lattice. Hence, a DNA chain that visits N lattice sites has exactly N potential binding sites. To account for the bending stiffness κ of the DNA chain, we assign a bending energy

$$H_{\mathrm{DNA}} = \frac{\kappa}{2\ell_0} \sum_{i=1}^{N-1} (\Delta \mathbf{r}_i)^2, \qquad [\mathbf{S1}]$$

where $\Delta \mathbf{r}_i$ is a vector describing the change in orientation of a DNA segment between sites i and $i+1$. Because our lattice model only allows for right-angle bends, $(\Delta \mathbf{r}_i)^2 = 2$ for a bend, and $(\Delta \mathbf{r}_i)^2 = 0$ otherwise.

Proteins can bind to the DNA and move between DNA binding sites, and DNA-bound proteins can interact with each other. The DNA binding energy of a protein, ϵ_i, may vary along the DNA. In our simulations we considered a chain with equivalent binding sites, or a chain with just one cognate *parS* site with a binding energy $\Delta\epsilon_{parS}$ relative to all other sites. The occupancy of a binding site i is described by ϕ_i, where $\phi_i = 1$ if the binding site is occupied by a protein and $\phi_i = 0$ otherwise.

1.1. Protein–Protein Interactions. Our model allows for two distinct types of interactions between proteins on the DNA: 1D spreading interactions with a strength J_S between proteins bound to sequential binding sites on the DNA chain and 3D bridging interactions with strength J_B between proteins bound to nonsequential DNA sites. Such bridging interactions are only possible when nonsequential DNA binding sites at which proteins are bound are nearest neighbors in 3D. The spreading interactions are directed along the DNA and are thus independent of the 3D conformation of the DNA. By contrast, the formation of bridging bonds depends sensitively on the 3D DNA conformation.

This model encompasses the freedom to choose the number of spreading and bridging interaction domains on each protein. Because we defined the system on a cubic lattice, the general model allows at most two spreading and four bridging interactions per protein. For example, in the spreading and bridging model there are two spreading interactions, but only one bridging interaction per protein, whereas in the dimer model each protein can engage in only one spreading interaction and no bridging interactions. Thus, in general a protein can only form a limited number of interactions at a time. To account for this constraint in our model, we assign oriented interaction domains to the proteins. Each spreading domain is oriented in either of the two directions along the DNA chain, and each bridging domain is oriented in one of the four remaining directions. Furthermore, two interaction domains on the same protein cannot be oriented in the same direction simultaneously. Importantly, interactions between proteins are only possible when the interaction domains of the two proteins are oriented to face each other.

The energies of the spreading and bridging interactions, as well as the DNA binding energy of the proteins, yield the total interaction energy:

$$H_{\mathrm{int}} = J_S \sum_{i=1}^{N-1} g_{i,i+1} \phi_i \phi_{i+1} + J_B \sum_{\langle ij \rangle_{3D}} g_{ij} \phi_i \phi_j. \qquad [\mathbf{S2}]$$

Here, the second sum only runs over nonsequential DNA sites, which are nearest-neighbor sites in 3D space. Interactions between proteins are only possible when the associated interaction domains of the proteins are oriented to face each other. If the two respective domains on neighboring proteins at sites i and j are favorably aligned such that a bond can form $g_{ij} = 1$ (proteins interact), and otherwise $g_{ij} = 0$ (no interaction).

Our Monte Carlo procedure consists of a set of DNA and protein moves, as detailed below. We used the Metropolis algorithm to accept or reject moves based on the change in energy associated with the move. Contributions to this change in energy may include the bending energy of the DNA, the binding energy of the proteins, and the protein–protein interaction energy, as described by Eqs. **S1** and **S2**.

1.2. DNA Moves. To sample DNA configurations we use a combination of local and nonlocal moves. The local moves include the corner and crankshaft moves commonly used in lattice polymer models (Fig. S1 *A* and *B*). We supplement this local move set with a collection of nonlocal moves designed to efficiently simulate dense polymer configurations. Local moves, such as the corner and crankshaft moves, require conformation changes in which polymer sites move from occupied to unoccupied sites. However, when the polymer is highly condensed such moves will frequently be impossible because two DNA sites cannot occupy the same location in space. To address this issue, a set of moves was designed to change the polymer conformation without altering the occupancy of the polymer sites in space. Thus, these moves result in sampling new configurations by rewiring the polymer, as illustrated in Fig. S1 *C–E*. This long-range move set is described in detail in ref. 1. Importantly, if there is a *parS* site located in the center of the DNA with a larger ParB binding affinity, such a nonlocal polymer move can amount to a relocation of this *parS* site to maintain its genomic position in the center of the DNA. We account for this by including the change in the energies for ParB binding to the DNA that would result from the nonlocal move.

As a consistency check, we confirmed that this combination of local and nonlocal polymer moves yields the well-known equilibrium properties for self-avoiding polymers with varying degrees of self-attraction between polymer sites. Specifically, we confirmed the expected scaling of the radius of gyration with the molecular weight of the polymer and the scaling of the average 3D distance between two sites on the polymer as a function of their distance measured along the polymer chain.

1.3. Protein Moves. We used a variety of protein moves. First, we used a binding move, in which a protein can either bind to an unoccupied DNA site or unbind from an occupied DNA site (Fig. S1*F*). We control the protein binding properties with a chemical potential for the proteins in solution. We can fix the concentration of proteins in solution by fixing this chemical potential. Alternatively, we can fix the total number of proteins in the system and account for the titration of ParB protein out of the cytoplasm by adjusting this chemical potential when proteins bind to or unbind from the DNA. Second, we used a hop move in which we attempt to move a protein from one site on the DNA to a randomly chosen other site (Fig. S1*G*). Third, we used a "bond change" move. Even when the DNA configuration and

the proteins are fixed in space, there may be multiple possible bonding configurations. Thus, we also used a bond change move in which all existing protein bonds at a given DNA site are broken and a random selection is made from all possible local bond configurations (Fig. S1*H*).

2. Binding Isotherms

To further quantify the different behavior of the five models described in the main text, we calculated binding isotherms, with the same interaction parameters as in Fig. 2. The binding curves describe the average fraction of binding sites occupied by ParB proteins on a DNA chain (without a *parS* site) in equilibrium with a solution of ParB dimers at fixed temperature. The proteins are assumed to be in excess and the free protein concentration was varied. The first four models all exhibited sigmoidal, Hill-like binding curves (Fig. S2). By contrast, the spreading and bridging model yielded a sharp vertical jump.

One expects the steepness of the binding curve to increase with the degree of cooperativity of protein binding. A vertical jump, as we observed for the spreading and bridging model, indicates cooperativity among all proteins binding to the available sites on the DNA. This behavior corresponds to a first-order phase transition in the large-N limit, similar to the transition between vapor and water at atmospheric pressures. What are the implications of such an all-or-nothing condensation transition for the cell? At very low ParB concentration, the ParB proteins would be dissolved, that is, dispersed throughout the cytoplasm and scattered on the DNA. By contrast, under normal conditions the ParB concentration would exceed this threshold, and the majority of ParB proteins would condense to form large protein–DNA clusters, limited in size by the total number of available ParB proteins or, possibly, by constraints on the condensation of the DNA, such as tethering.

3. Triangular Binding Profiles

For a sufficiently strong *parS* site, we observed that the vast majority of ParB proteins localize around the *parS* site in the spreading and bridging model. In this case, the average ParB binding profile exhibits a triangular shape centered around the *parS* site: The ParB binding probability is ∼1 at the *parS* site, and decays to nearly 0 a distance M_c from the *parS* site, where M_c is the total number of proteins in the cluster (Fig. 3*A*).

The triangular ParB binding profile is consistent with the formation of a single large ParB–DNA cluster; the cluster as a whole can shift over a range of sites along the DNA as long as it overlaps with the *parS* site. The triangular shape of the profile can be understood by noting that the probability for ParB binding at a particular site is proportional to the number of states in which the ParB–DNA cluster overlaps with that site. The number of states in which a cluster with M_c proteins overlaps with a given site at a genomic distance s from the *parS* site scales as $\sim M_c - s$ (when $s \le M_c$), thus giving rise to a triangular binding ParB profile. Note that significant deviations from this triangular binding profile occur in parameter regimes for which the cluster includes multiple unoccupied DNA loops (Fig. 3*C*, *Inset*).

4. Loop Statistics

In this section we describe the statistics of DNA loops that emanate from the ParB–DNA cluster. Fig. S3 shows the loop-size distribution for the spreading and bridging model. The probability $p(s)$ to form a loop of size s exhibits a power-law decay. These results can be understood by noting that this distribution is determined by the entropic cost of forming a loop of size s: $S_{\mathrm{loop}}(s) \sim k_{\mathrm{B}} \ln(s^{3\nu})$ (2), where $\nu \approx 0.588$ is the Flory exponent (3). This dependence of the loop entropy on loop size implies a universal loop-size distribution, $p(s) \sim s^{-3\nu}$, independent of cluster size M_c or the spreading bond strength J_S, consistent with our simulation results (Fig. S3).

The loop-size distribution implies that the average loop length $\langle \ell \rangle$ is insensitive to protein–protein bond strengths or ParB cluster size, in agreement with our simulation results shown in Fig. S4*A*. However, the average loop length does depend on the total length of the DNA:

$$\langle \ell \rangle = \frac{(3\nu - 1)\left(N^{3\nu} - N^2\right)}{(3\nu - 2)(N^{3\nu} - N)}. \qquad [S3]$$

For a DNA strand with $N = 1{,}000$ binding sites, we expect $\langle \ell \rangle \approx 13$, consistent with our simulations (Fig. S4*A*).

4.1. Scaling Behavior of the Number of Loops. Because loops are formed at the cluster surface, the average number of loops $\langle N_{\mathrm{loops}} \rangle$ should increase with the surface area of the cluster, which increases with cluster size. In particular, the number of surface sites of a cluster is expected to increase as $M_{\mathrm{surface}} \sim M_c^{\alpha}$. One expects $\alpha = 2/3$ for a 3D spherical cluster and $\alpha = 1$ for, say, a 1D filamentous cluster, which is all surface. To test this prediction for the surface-area scaling, we defined as a surface site any site occupied by a protein with fewer than the maximal number of six proteins at neighboring sites and measured the average number of such surface sites for different cluster sizes M_c. Indeed, for a model with two spreading and four bridging interactions per protein we found $\alpha = 2/3$, which indicates a compact, spherical cluster (Fig. S5). By contrast, for the spreading and bridging model we found that $M_{\mathrm{surface}} \sim M_c^{\alpha}$ with an exponent $\alpha \approx 0.9$, indicating a more extended cluster with fractal surface area, as shown in Fig. S5.

The scaling of the surface area with cluster size implies that $\langle N_{\mathrm{loops}} \rangle \sim M_c^{\alpha}$. In addition, $\langle N_{\mathrm{loops}} \rangle$ should also depend on the spreading bond strength J_S, because the formation of a loop from the ParB–DNA cluster requires breaking a spreading bond. Taking the corresponding Boltzmann factor together with the expected surface area scaling yields

$$\langle N_{\mathrm{loops}} \rangle \sim \exp(-J_S / k_{\mathrm{B}}T) M_c^{\alpha}. \qquad [S4]$$

To test this prediction within the spreading and bridging model, we determined the average number of loops in a ParB cluster as a function of cluster size M_c and the strength of the spreading bond J_S, as shown in Fig. S4*B*. Indeed, we find that $\langle N_{\mathrm{loops}} \rangle \sim M_c^{\alpha}$ with an exponent $\alpha \approx 0.9$. Furthermore, we observe that $\langle N_{\mathrm{loops}} \rangle \sim \exp(-J_S / k_{\mathrm{B}}T)$, consistent with the theoretical prediction.

4.2. Scaling Behavior of Gene-Silencing Profiles. How can we understand the scaling of the ParB binding profile (Fig. 4 *B* and *D*), and how is it affected by looping? Because the formation of a loop requires breaking a spreading bond, reducing the magnitude of J_S increases the average number of loops. Indeed, weakening J_S from $-8k_{\mathrm{B}}T$ to $-6k_{\mathrm{B}}T$ causes the ParB binding profile to deviate more strongly from a triangular shape owing to an increase in DNA looping, as shown in Fig. 4*A*. Surprisingly, these binding profiles can still be collapsed by scaling with cluster mass M_c. In the absence of loops, the average footprint L of the ParB–DNA cluster (Fig. 4*B*) is simply set by total number of proteins in the cluster M_c. However, the presence of loops extruding from the cluster will increase the average 1D range of binding sites that contribute to the 3D cluster. Thus, the ParB cluster footprint L has two contributions: a contribution from the total number of proteins in the cluster M_c and a contribution from the accumulated length in loops. However, because the total loop length only scales sublinearly with cluster mass (total loop length $\sim M_c^{\alpha}$ with $\alpha \approx 0.9$), the loop contribution becomes

negligible for large enough M_c. Indeed, for all our simulations we find that the DNA footprint L of the ParB cluster scales approximately linearly with the number of proteins in the cluster, despite the presence of loops. It is this property of the modeled ParB cluster that allows for the simple data collapse shown in Fig. 4 *B* and *D*; this collapse demonstrates that the DNA exposure at a specific location is governed by the ratio of the footprint L of the ParB–DNA complex to the genomic distance from the *parS* site.

To further investigate the effect of looping on DNA exposure, we generated three datasets using the spreading and bridging model with the strength of a spreading bond set to $J_S = -8k_BT$, $-6k_BT$, and $-4k_BT$; we expect the largest effects due to looping for $J_S = -4k_BT$. Interestingly, the DNA exposure at *parS*-proximal sites is dramatically enhanced and exhibits a weaker decay with (ParB expression level)/(*parS* distance) for the system with abundant looping ($J_S = -4k_BT$), as shown in Fig. 4*D*. The results with $J_S = -8k_BT$ with sparse looping predict that the exposure depends on (ParB expression level)/(*parS* distance) with a power law exponent of -1 (Fig. 4*D*), consistent with the behavior observed in P1 plasmids (Fig. 4*F*) (4).

5. Roadblock Simulations

In the main text we investigated how the ParB binding profile for a system with a roadblock placed immediately to the left of a *parS* site depends on the size of the ParB cluster M_c (Fig. 3*D*). Here we provide a scaling argument leading to a prediction that the probability p_{left} to the left of the roadblock scales as $p_{\text{left}} \sim M_c^{\alpha}$.

In the absence of a roadblock, the ParB–DNA cluster can shift up to $\sim M_c$ binding sites to the left while still overlapping with the *parS* site. Thus, the probability for ParB binding close to the left of *parS* site is proportional to these $\sim M_c$ possible configurations. However, in the presence of a roadblock, we should only consider the fraction $\langle \ell \rangle N_{\text{loops}}/M_c \sim M_c^{\alpha-1}$ of the configurations for which a loop is actually formed at the position of roadblock. Thus, $p_{\text{left}}(d) \sim M_c M_c^{\alpha-1} = M_c^{\alpha}$ (for $d < M_c$), consistent with the results shown in Fig. 3*D*, *Inset* for the spreading and bridging model ($\alpha = 0.9$). As a consistency check, we considered a model in which each protein can form two spreading bonds and four bridging bonds. Owing to the larger number of bridging bonds in this model, we find that the clusters become more spherical, resulting in a lower value of the loop exponent $\alpha \approx 2/3$ (Figs. S5 and S6). Thus, for this model, we would expect that $p_{\text{left}} \sim M_c^{2/3}$, which is consistent with the simulation results shown in Fig. S6, *Inset*.

6. DNA Confinement

To investigate the effects of DNA confinement on the formation of protein–DNA clusters, we performed Monte Carlo simulations with confined DNA for the bridging model, the spreading or bridging model, and the spreading and bridging model. We used a simple harmonic DNA confinement potential of the following form:

$$V_{\text{conf}} = \frac{1}{2}\sum_{i=1}^{N} k_{\text{conf}}(r_i - R_0)^2 \theta(r_i - r_0). \qquad \textbf{[S5]}$$

Here, k_{conf} is the strength of the confinement potential, r_i measures the distance from site i to the origin, and R_0 is the confinement radius. The Heaviside step-function $\theta(r)$ ensures that the confinement potential only contributes when $r \geq R_0$. Using $k_{\text{conf}} = 2k_BT$ and $R_0 = 7$, roughly 2.5 times less than the equilibrium radius of gyration without confinement for a chain of length $N = 500$, we performed simulations to determine the cluster-size distribution and the ParB binding profiles for the bridging model, the spreading or bridging model, and the spreading and bridging model in the presence of DNA confinement. The results of the simulations with confinement (Fig. S7 *A* and *B*) are qualitatively similar to the results for the cluster-size distribution and ParB binding profiles in the absence of DNA confinement (Figs. 2*F* and 3*A*).

7. Nucleation Kinetics

ParB foci do not form in cells where the *parS* site is absent (Fig. 5). This suggests that *parS* is crucial for the nucleation of ParB complexes on the DNA. In the main text we showed that a *parS*-induced reduction of the nucleation barrier ΔF_{parS} is required to satisfy the condition $\exp(-\Delta F_{parS}) < N$ for simple nucleation to occur reliably at a single *parS* site and not at any of the N nonspecific sites. Thus, this would require $\Delta F_{parS} \approx -12k_BT$. By contrast, if nucleation were to occur through the formation of a bond between two ParB dimers bound to distinct, but nearby, *parS* sites (as occurs during replication), this condition would become $\exp(-\Delta F_{parS}) < N^2$, requiring roughly $\Delta F_{parS} \approx -6k_BT$. However, we showed experimentally that a single *parS* site per cell is sufficient for the formation of ParB foci on the DNA (Fig. 5), ruling out the scenario that ParB foci formation requires the presence of two nearby *parS* sites.

8. Equilibrium Properties of a Two-State Model for ParB

In *Discussion* we describe a two-state model in which a ParB dimer can be in two different states (closed and inert, or open and capable of forming interactions), and we focused on the implications that such a two-state model might have on the kinetics of cluster nucleation. Interestingly, as discussed below, the equilibrium behavior of such a model is not qualitatively different from the one-state models (in which the protein is always in the open state) discussed in *Results* in the main text.

For a two-state model for ParB, suppose the energy of the open state is E_0 higher than that of the closed state, except when the protein is bound at a *parS* site, in which case the open and closed states have, say, the same energy. To form clusters, the proteins must be in the open state. Thus, in this two-state model the energy of a cluster is increased by $\Delta E = (M_c - 1)E_0$ relative to the energy of the cluster in the one-state model if the cluster is formed around a *parS* site (localized), and $\Delta E = M_c E_0$ if the cluster is formed with all of the proteins bound to nonspecific sites (delocalized). This has two implications:

i) The cluster has an additional energetic contribution to localization at a *parS* site within a two-state model, because the energy of a cluster localized at a *parS* site (Eq. **2**) is reduced by E_0 relative to a nonlocalized cluster, i.e., $\Delta F_{parS} = \Delta\epsilon_{parS} - E_0$.

ii) In the two-state model, a cluster is destabilized by an energy $M_c E_0$. Importantly, the total cohesive energy E_{coh} from the (spreading and bridging) bonds that hold the cluster together also scale with M_c in the same way, that is, $E_{\text{coh}} \sim (3/2)JM_c$. For the sake of simplicity we can assume that the spreading and bridging bonds have the same strength ($J_B = J_S = J$). Thus, the cluster energies per protein in the two-state model are reduced by an amount E_0 per protein compared with the one-state model. Put simply, the cluster energies of the two-state model with bond strength J are the same as the cluster energies of a one-state model with bond strength $J + 2E_0/3$. Thus, this essentially amounts to the same model, but with a redefined bond strength.

From this analysis, we conclude that the two-state model will have the same equilibrium properties at the one-state model, including cluster sizes and silencing profiles, and will still require three interaction domains per protein to stabilize the clusters.

9. Variety of Models with Spreading and/or Bridging Interactions Do Not Result in the Formation of ParB Condensates

One could envision other simple models with just a few interaction domains that are not discussed in *Results* in the main

text. These other options are not explicitly addressed either because they will show equivalent behavior to the models we did discuss or because one can argue a priori that they are not consistent with experiments.

Models with multiple bridging domains per protein could possibly form condensates, but if they do not also have two spreading domains such models will not be capable of explaining the roadblock experiments. We find that if the proteins have two spreading domains, only one additional bridging domain is required to form ParB condensates (as in the spreading and bridging model).

A model with a single spreading and a single bridging domain is part of a larger class of models (to which the bridging model and the spreading or bridging models also belong) that fails to result in a condensed ParB–DNA complex. At root, this type of model with only two binding sites per ParB does not allow for a 3D surface tension, which is required to drive condensation. In all such models, proteins can interact to form small clusters in which all of the bonds (or all but two) are satisfied, and, because of entropy, the formation of many small clusters is more favorable than formation of a single large cluster.

SI Materials and Methods

Live Cell Imaging and Image Analysis. Fluorescence microscopy was performed with a Nikon Ti microscope equipped with Plan Apo 100×/1.4 N.A. phase contrast oil objective and a CoolSnapHQ2 CCD camera (Photometrics). Cells were immobilized on 2% (vol/vol) agarose pads containing growth media. DNA was visualized with DAPI (2 μg/mL) (Molecular Probes). Images were cropped and adjusted using MetaMorph software (Molecular Devices). Final figure preparation was performed in Adobe Illustrator.

Immunoblot Analysis. Cells were grown exponentially at 30 °C and shifted to 42 °C for 1.5 h. Then IPTG was added to a final concentration of 0.5 mM to induce the expression of GFP-Spo0J and GFP-Spo0J (G77S) at 42 °C. Samples were harvested immediately before and 0.5 h after induction. Cultures were diluted with prewarmed media when needed to make sure the OD_{600} of the cultures was below 0.6 at all times. Whole-cell lysates were prepared as described (5). Samples were heated for 5 min at 80 °C before loading. Equivalent loading was based on OD_{600} at the time of harvest. Proteins were separated by SDS/PAGE on 12.5% polyacrylamide gels, electroblotted onto Immobilon-P membranes (Millipore), and blocked in 5% nonfat milk in PBS containing 0.5% Tween-20. The blocked membranes were probed with anti-GFP (1:10,000) (6) or anti-SigA (1:10,000) (7), diluted into 3% BSA in PBS–0.05% Tween-20. Primary antibodies were detected using horseradish peroxidase-conjugated goat anti-rabbit IgG (BioRad) and the Super Signal chemiluminscence reagent as described by the manufacturer (Pierce).

Plasmid Construction. pNS040 [*amyE::parS (kan)*] was constructed by annealing oTD40 and oTD41 and inserting this fragment into pER82 [*amyE::kan*] at BamHI site.

pWX589 [*yvbJ::Pspank-gfp-spo0J (ΔparS) (cat)*] was generated by cloning *gfp-spo0J (ΔparS)* [PCR-amplified from pKM256 (8) using oWX998 and oWX999 and digested with XmaI and NheI] into pER134 [*yvbJ::Pspank (cat)*] between XmaI and NheI.

pWX624 [*yvbJ::Pspank-gfp-spo0J (G77S) (ΔparS) (cat)*] was generated from pWX589 by site-directed mutagenesis using primers oTG049F and oTG049R.

Strain Construction. Δ*spo0J (ΔparS)::spec* was obtained by direct transformation of an isothermal assembly product (9) into the wild-type strain PY79. The isothermal assembly reaction contained three PCR fragments: (*i*) a 0.7-kb region upstream the *spo0J* gene (amplified from wild-type genomic DNA using primers oWX507 and oWX886); (*ii*) *loxP-spec-loxP* cassette (amplified from pWX466 using primers oWX438 and oWX439), and (*iii*) a 1.6-kb region downstream of the *spo0J* gene (amplified from wild-type genomic DNA using primers oWX887 and oWX888). pWX466 contains a *loxP-spec-loxP cassette*. The resulting construct was sequenced across the *soj-spo0J* region using primers oWX507 and oWX508. This construct deletes the *parS* site that is within the *spo0J* gene, whereas Δ*spo0J::spec* in AG1468 (10) retains the *parS* site at this locus.

1. Deutsch JM (1997) Long range moves for high density polymer simulations. *J Chem Phys* 106(21):8849–8854.
2. de Gennes P-G (1979) *Scaling Concepts in Polymer Physics* (Cornell Univ Press, Ithaca, NY).
3. Le Guillou JC, Zinn-Justin J (1977) Critical exponents for the n-vector model in three dimensions from field theory. *Phys Rev Lett* 39(2):95.
4. Rodionov O, Lobocka M, Yarmolinsky M (1999) Silencing of genes flanking the P1 plasmid centromere. *Science* 283(5401):546–549.
5. Doan T, Rudner DZ (2007) Perturbations to engulfment trigger a degradative response that prevents cell-cell signalling during sporulation in Bacillus subtilis. *Mol Microbiol* 64(2):500–511.
6. Rudner DZ, Fawcett P, Losick R (1999) A family of membrane-embedded metalloproteases involved in regulated proteolysis of membrane-associated transcription factors. *Proc Natl Acad Sci USA* 96(26):14765–14770.
7. Fujita M (2000) Temporal and selective association of multiple sigma factors with RNA polymerase during sporulation in Bacillus subtilis. *Genes Cells* 5(2):79–88.
8. Sullivan NL, Marquis KA, Rudner DZ (2009) Recruitment of SMC by ParB-parS organizes the origin region and promotes efficient chromosome segregation. *Cell* 137(4):697–707.
9. Gibson DG, et al. (2009) Enzymatic assembly of DNA molecules up to several hundred kilobases. *Nat Methods* 6(5):343–345.
10. Ireton K, Gunther NW, 4th, Grossman AD (1994) spo0J is required for normal chromosome segregation as well as the initiation of sporulation in Bacillus subtilis. *J Bacteriol* 176(17):5320–5329.

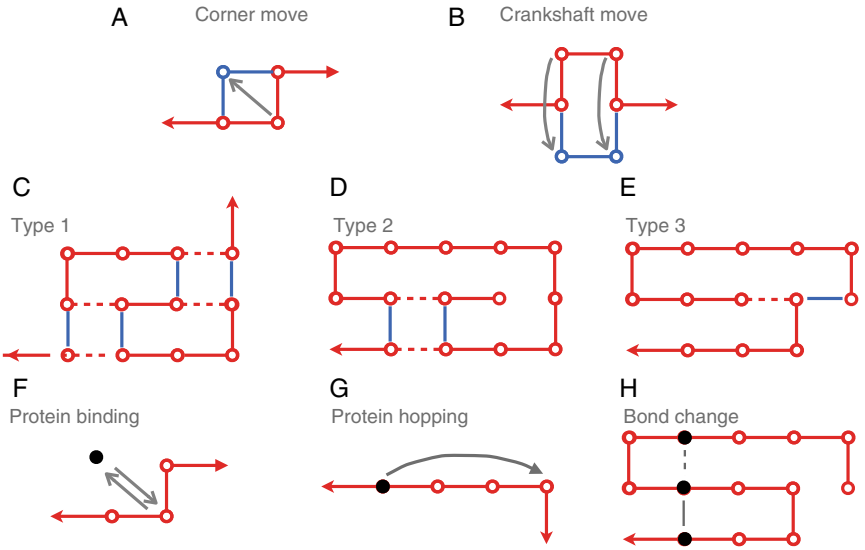

Fig. S1. Monte Carlo move set. (*A* and *B*) Local corner and crankshaft polymer moves. The nonlocal polymer moves (*C*–*E*) are described in detail in ref. 1. Dashed red polymer connections are broken and solid blue connections are formed. Arrows indicate continuation of the polymer chain. (*F*–*H*) Depiction of the protein moves, including binding moves, hopping moves, and bond change moves.

1. Deutsch JM (1997) Long range moves for high density polymer simulations. *J Chem Phys* 106(21):8849–8854.

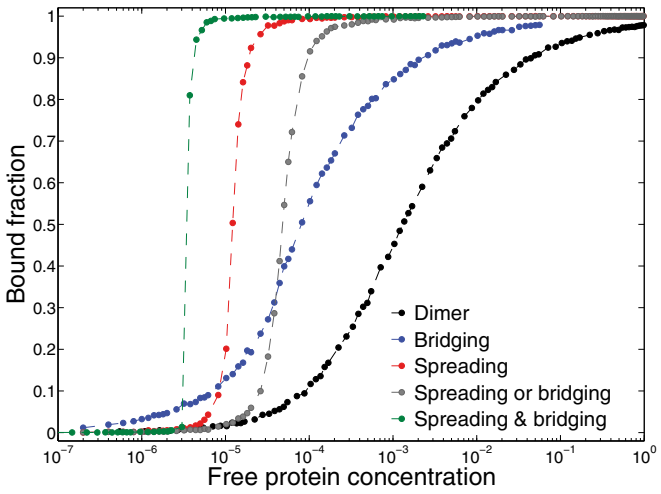

Fig. S2. Binding isotherms. The fraction of DNA sites bound by proteins as a function of the concentration of free protein dimers in solution (in arbitrary units). The first four models exhibit a sigmoidal, Hill binding curve with varying degrees of cooperativity, whereas the spreading and bridging model exhibits a sharp vertical jump indicative of a first-order phase transition. In all models, the proteins are assumed to be dimerized in solution.

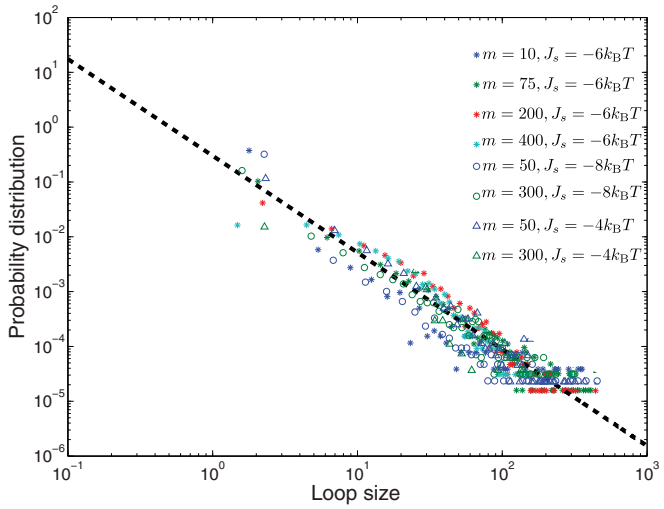

Fig. S3. DNA loop-size distribution. The probability distribution for the size of unoccupied DNA loops emanating from the ParB–DNA cluster in the spreading and bridging model. The dashed line indicates a slope of $-3\nu \approx -1.764$, indicating that the probability to form a loop decays with loop size as a power law with an exponent consistent with 3ν, where $\nu \approx 0.588$. These results were obtained from simulations using a DNA strand with $N = 1{,}000$ binding sites, bridging bond strength $J_B = -6k_BT$, and the total number of ParB proteins m and the spreading bond strength J_S as indicated in the key.

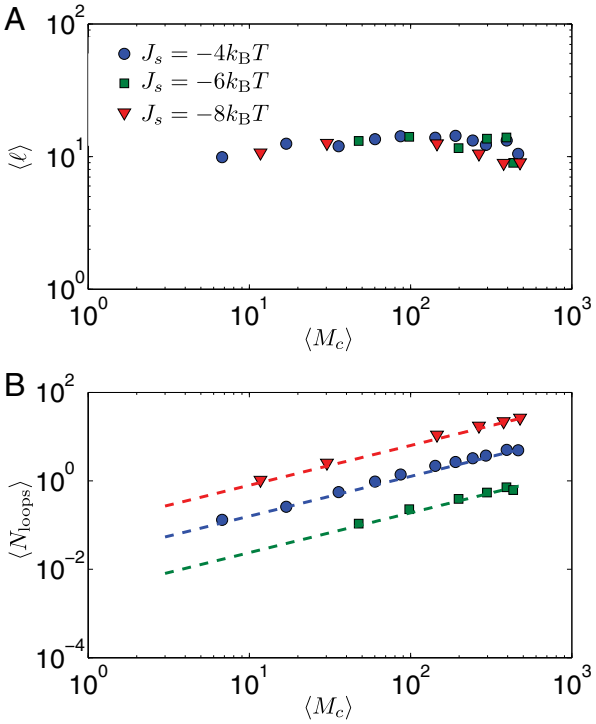

Fig. S4. Loop statistics. (*A*) The average loop length $\langle \ell \rangle$ as a function of the average cluster size M_c for the spreading and bridging model. (*B*) The average number of loops emanating from the ParB–DNA cluster $\langle N_{\text{loops}} \rangle$ as a function of the average cluster size M_c. The dashed lines indicate the scaling behavior $\langle N_{\text{loops}} \rangle \sim \exp(-J_S k_B T) < M_c^0.9$, where J_S is the spreading bond strength. These results were obtained from simulations on a DNA strand with $N = 1{,}000$ binding sites, bridging bond strength $J_B = -6k_BT$, and the spreading bond strength J_S as indicated in the key in *A*.

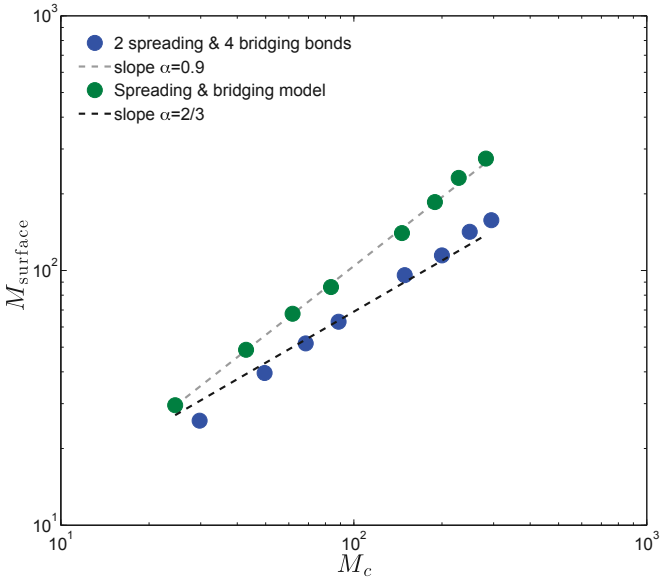

Fig. S5. Cluster surface area scaling and the loop exponent. The average number of surface sites in the cluster $M_{surface}$ as a function of the average cluster size M_c for a model with two spreading and four bridging interactions per protein (blue) and for the spreading and bridging model (green). A surface site in the cluster is defined as an occupied site in the cluster with fewer than the maximum number of six neighbors. These data are consistent with the prediction that $M_{surface} \sim M_c^{\alpha}$, where $\alpha \approx 0.9$ for the spreading and bridging model and $\alpha = 2/3$ for a model with two spreading and four bridging interactions per protein. The lower value for the loop exponent in the latter case is expected because a higher number of bridging interactions leads to the formation of a more compact spherical cluster.

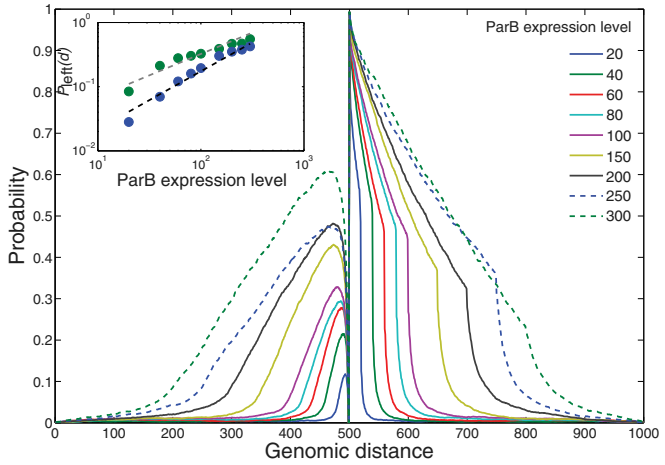

Fig. S6. Roadblock simulations. Probability of a bound protein versus genomic position with a roadblock inserted immediately to the left of the *parS* site at the center of the DNA chain, for a model with two spreading and four bridging domains per protein. The total number of ParB proteins on the DNA is varied, and a larger number of ParB proteins results in a more symmetric binding profile. (*Inset*) The binding probability, $p_{left}(d)$, at a position $d = 15$ binding sites to the left of the roadblock as a function of ParB expression level. Green data points are simulation results for a model with two spreading and four bridging interaction domains per protein and the blue data points are simulation results for the spreading and bridging model, which has only one bridging domain per protein. The gray dashed line indicates power-law scaling with an exponent of $2/3$, and the black dashed line indicates an exponent of 0.9.

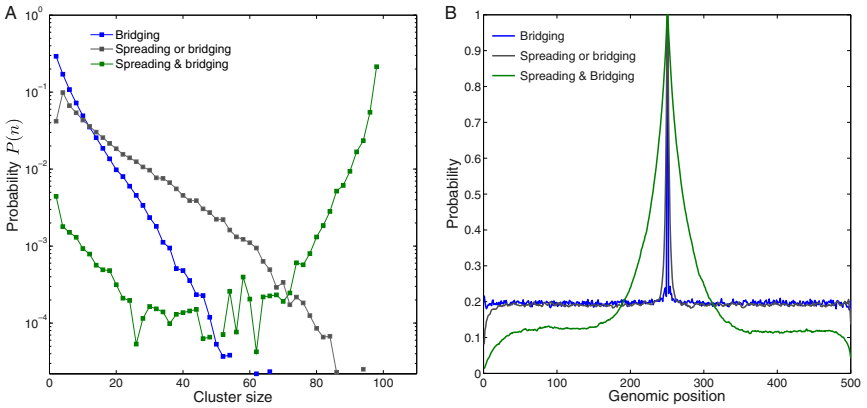

Fig. S7. Effects of DNA confinement on cluster-size distributions and ParB binding profiles. (*A*) Probability distribution $P(n)$ for a DNA-bound protein to be part of a cluster of size n. A harmonic potential is included to confine the DNA, with the parameters $k_{conf} = 2k_BT$ and $R_0 = 7$, roughly 2.5 times less than the equilibrium radius of gyration without confinement for the chain of length $N = 500$. All other parameters are as in Fig. 2*F*. (*B*) Probability of a bound protein versus genomic position with a strong *parS* site at the center of the DNA (parameters as in Fig. 3*A* with the addition of a confinement potential as in *A*).

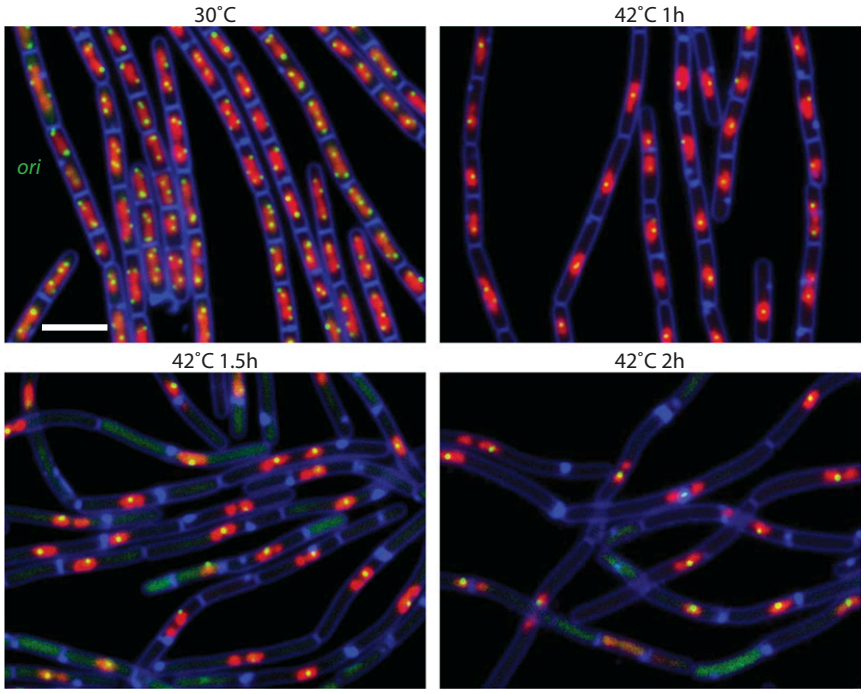

Fig. S8. Growth of *dnaB(ts)* at 42 °C for 1.5 h is sufficient to generate 1-N content nucleoids. Cells (BWX925) harboring a *dnaB(ts)* allele were grown at 30 °C and shifted to 42 °C for indicated times. After 1.5 h, greater than 90% of cells ($n = 1,221$) had 1-N DNA content as assessed by the presence of a single origin focus. DAPI-stained nucleoids were false-colored red. Membranes were stained with FM4-64 (3 μg/mL) and false-colored blue. The replication origin was labeled using a *tetO* array inserted at −7° bound by TetR-CFP and false-colored green. (Scale bar, 4 μm.)

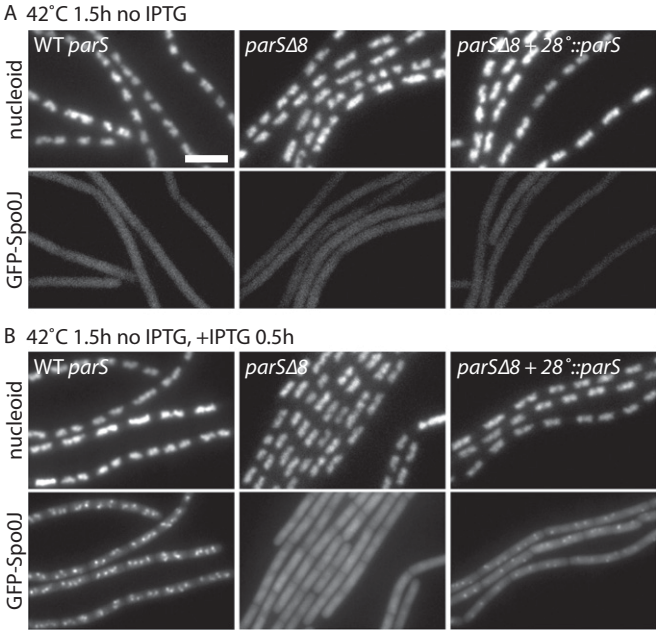

Fig. S9. GFP-Spo0J form foci in cells harboring *parS* sites at 42 °C. (*A*) Representative images of cells with all eight wild-type *parS* sites (BWX2434, WT *parS*, first panel); none of the eight endogenous *parS* sites (BWX2436, *parS* Δ8, second panel); or *parS* Δ8 with an ectopic *parS* site inserted at 28 (*amyE*) (BWX2438 and BWX2783, *parS* Δ*8*+*28*°*::parS*, third and fourth panels) grown at 30 °C in the absence of IPTG and shifted to 42 °C for 1.5 h. GFP-Spo0J (first to third panels) or GFP-Spo0J (G77S) (fourth panel) was under the control of IPTG-inducible promoter. After 1.5 h, IPTG was added to a final concentration of 0.5 mM. (*B*) One-half hour induction was enough to generate GFP-Spo0J foci in cells with *parS* sites. (Scale bar, 4 μm.)

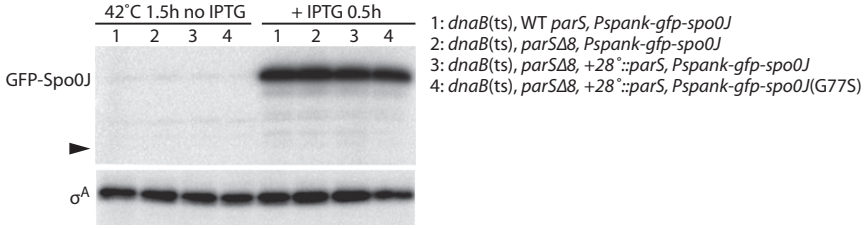

Fig. S10. GFP-Spo0J fusions were expressed at similar levels in the different strains. Immunoblot analysis of GFP-Spo0J and a loading control (σ^A) in cells that are shown in Fig. 5 *B* and *C*. The position on the gel where free GFP migrates is indicated (caret).

Table S1. Strains used in this study

Strain	Genotype	Source	Figure
BWX2454	*Δspo0J::spec, yvbJ::Pspank-gfp-spo0J (ΔparS) (cat), dnaB134 (ts) - zhb83::Tn917 (erm)*	This study	5
BWX2456	*parS Δ8, Δspo0J (ΔparS)::spec, yvbJ::Pspank-gfp-spo0J (ΔparS) (cat), dnaB134 (ts) - zhb83::Tn917 (erm)*	This study	5
BWX2458	*parS Δ8, amyE::parS (kan), Δspo0J (ΔparS)::spec, yvbJ::Pspank-gfp-spo0J (ΔparS) (cat), dnaB134 (ts) - zhb83::Tn917 (erm)*	This study	5
BWX2789	*parS Δ8, amyE::parS (kan), Δspo0J (ΔparS)::spec, yvbJ::Pspank-gfp-spo0J (G77S) (ΔparS) (cat), dnaB134 (ts) - zhb83::Tn917 (erm)*	This study	5
BWX925	*yycR(-7)::tetO48 (cat), pelB(+174)::lacO48 (kan), ycgO::PftsW-tetR-cfp (spec) terminators PftsW-lacI-mypet, dnaB134 (ts) - zhb83::Tn917 (erm)*		S8
BWX2434	*Δspo0J::spec, yvbJ::Pspank-gfp-spo0J (ΔparS) (cat)*	This study	S9
BWX2436	*parS Δ8, Δspo0J (ΔparS)::spec, yvbJ::Pspank-gfp-spo0J (ΔparS) (cat)*	This study	S9
BWX2438	*parS Δ8, amyE::(kan), Δspo0J (ΔparS)::spec, yvbJ::Pspank-gfp-spo0J (ΔparS) (cat)*	This study	S9
BWX2783	*parS Δ8, amyE::parS (kan), Δspo0J (ΔparS)::spec, yvbJ::Pspank-gfp-spo0J (G77S) (ΔparS) (cat)*	This study	S9
PY79	Wild-type	1	
AG1468	*Δspo0J::spec, trpC2, pheA1*	2	
BNS1657	*pars Δ8*	3	
KPL69	*dnaB134 (ts) - zhb83::Tn917 (erm), trpC2, pheA1*	4	

1. Youngman PJ, Perkins JB, Losick R (1983) Genetic transposition and insertional mutagenesis in Bacillus subtilis with Streptococcus faecalis transposon Tn917. *Proc Natl Acad Sci USA* 80(8):2305–2309.
2. Ireton K, Gunther NW, 4th, Grossman AD (1994) spo0J is required for normal chromosome segregation as well as the initiation of sporulation in Bacillus subtilis. *J Bacteriol* 176(17): 5320–5329.
3. Sullivan NL, Marquis KA, Rudner DZ (2009) Recruitment of SMC by ParB-parS organizes the origin region and promotes efficient chromosome segregation. *Cell* 137(4):697–707.
4. Rokop ME, Auchtung JM, Grossman AD (2004) Control of DNA replication initiation by recruitment of an essential initiation protein to the membrane of Bacillus subtilis. *Mol Microbiol* 52(6):1757–1767.

Table S2. Plasmids used in this study

Plasmid	Description	Source
pKM256	*pelB::Psoj-gfp-spo0J (ΔparS) (cat)*	1
pNS40	*pars Δ8, Δspo0J (ΔparS)::spec, yvbJ::Pspank-gfp-spo0J (ΔparS) (cat), dnaB134 (ts) - zhb83::Tn917 (erm)*	This study
pWX589	*yvbJ::Pspank-gfp-spo0J (ΔparS) (cat)*	This study
pWX624	*yvbJ::Pspank-gfp-spo0J (G77S) (ΔparS) (cat)*	This study

1. Sullivan NL, Marquis KA, Rudner DZ (2009) Recruitment of SMC by ParB-parS organizes the origin region and promotes efficient chromosome segregation. *Cell* 137(4):697–707.

Table S3. Plasmids used in this study

Oligos	Sequence	Use
oTD40	gatcaatcagaatgttacacgtgaaacaaagaaaaac	pNS40
oTD41	gatcgtttttctttgtttcacgtgtaacattctgatt	pNS40
oTG049F	tatgatattgttgcgagtgaacggcgttttc	pWX624
oTG049R	gaaaacgccgttcactcgcaacaatatcata	pWX624
oTG049R	gaaaacgccgttcactcgcaacaatatcata	pWX624
oWX438	gaccagggagcactggtcaac	Δ*spo0J* (Δ*parS*)::*spec*
oWX439	tccttctgctccctcgctcag	Δ*spo0J* (Δ*parS*)::*spec*
oWX507	cgtgcttgaattttcaattatttccc	Δ*spo0J* (Δ*parS*)::*spec*
oWX508	acccgttgcaaaggctcactgggcgc	Δ*spo0J* (Δ*parS*)::*spec*
oWX886	ctgagcgagggagcagaaggatcctttccaaggcctttagccattcgcagc	Δ*spo0J* (Δ*parS*)::*spec*
oWX887	gttgaccagtgctccctggtccgagaatcataaatgaaaaaaccatctttc	Δ*spo0J* (Δ*parS*)::*spec*
oWX888	agaggtaaacgtaatgctcgcaggcc	Δ*spo0J* (Δ*parS*)::*spec*
oWX998	aaaCCCGGGacataaggaggaactactatgagtaaagg	pWX589
oWX999	tttGCTAGCcagagtggaggcaagaacgccttaaccc	pWX589